photonics

MDPI

Communication

A High-Sensitivity Sensor Based on Insulator-Metal-Insulator Structure

Xiaoying Chen [1,2,3], Zhuozhen Gao [1,2,3], Zhiqi Li [1,2,3], Jingjing Wang [1,2,3], Hui Wang [1,2,3], Sixue Chen [1,2,3], Jian Shen [1,2,3,*] and Chaoyang Li [1,2,3,*]

1 School of Information and Communication Engineering, Hainan University, Haikou 570228, China; 21220854000136@hainanu.edu.cn (X.C.); gaozhuozhen@hainanu.edu.cn (Z.G.); 21210810000015@hainanu.edu.cn (Z.L.); 21220854000174@hainanu.edu.cn (J.W.); 21220854000171@hainanu.edu.cn (H.W.); sixuechen@hainanu.edu.cn (S.C.)
2 School of Computer Science and Technology, Hainan University, Haikou 570228, China
3 State Key Laboratory of Marine Resource Utilization in South China Sea, Hainan University, Haikou 570228, China
* Correspondence: shenjian@hainanu.edu.cn (J.S.); lichaoyang@hainanu.edu.cn (C.L.)

Abstract: In this paper, a theoretical model of a surface plasmon resonance (SPR) biosensor based on the insulator-metal-insulator (IMI) structure is proposed. The sensor mainly consists of two IMI structures, $MgF_2/Au/Al_2O_3$ and Al_2O_3/Au/sensing medium structure, respectively. Benefits from the symmetrical modes stimulated by the IMI structure, i.e., the electric field strength inside the sensing medium, are reinforced, resulting in a better overall performance in sensitivity and figure of merit (FOM). The influences of the thickness of the metal layers, the parameters of the dielectric layer materials, and the number of structural layers on the performance of this sensor are discussed. When the refractive index (RI) of the analyte varies in the range of 1.3494–1.3495, the optimized sensor could achieve a maximum wavelength sensitivity of 220 μm/RIU (refractive index unit) and a FOM of 3013.70 RIU^{-1}. Compared with the conventional SPR sensor, the sensitivity and FOM of this structure are significantly improved.

Keywords: surface plasmon resonance; IMI structure; sensitivity; figure of merit

Citation: Chen, X.; Gao, Z.; Li, Z.; Wang, J.; Wang, H.; Chen, S.; Shen, J.; Li, C. A High-Sensitivity Sensor Based on Insulator-Metal-Insulator Structure. *Photonics* **2023**, *10*, 502. https://doi.org/10.3390/photonics10050502

Received: 24 March 2023
Revised: 12 April 2023
Accepted: 20 April 2023
Published: 26 April 2023

1. Introduction

In recent years, optical refractive index sensors have received much attention in chemical and biological sensing because of their small size, corrosion tolerance, high accuracy, and resistance to interference [1–3]. Surface plasmon resonance sensors are among the most critical sensor types used for direct label-free observation of biomolecular interactions [4]. The conceptualization of SPR sensor research started more than 80 years ago with the phenomenon first observed by Wood [5] until the first introduction of gas sensing and biosensing principles by Liedberg et al. [6]. Over the past three decades, SPR sensor technology has made significant advances and realized several applications in chemical sensing, food-borne marker screening, environmental monitoring, and medical diagnostics [7–9]. In 2001, Nenninger et al. [4] presented a Teflon-based SPR sensor for RI sensing, and the sensitivity was 30 μm/RIU. In 2016, Sreekanth et al. [10] proposed a plasmon biosensor based on hyperbolic metamaterials with a high sensitivity of 30 μm/RIU to detect the picomolar concentration of biomolecules with ultra-low molecular weights. In 2017, Feng et al. [11] theoretically analysed some parameters of side-polished fibre-based SPR sensor, LRSPR sensor, and symmetrical LRSPR sensor using a finite element method to explore the advantages of MgF_2-based LRSPR sensor. The sensitivity was 5.28 μm/RIU. A surface plasmon is an electron sparsity wave generated by the collective oscillation of free electrons in metals interacting with photons and propagating along the metal-dielectric surface. This transverse electromagnetic wave is called a surface plasma wave (SPW). When

the wave vector and frequency of the incident p-polarized light match the wave vector and frequency of the SPW, the two light waves resonate. Moreover, the resonance conditions depend on the angle of incidence, the wavelength of the incident light, and the dielectric constants of the metal and dielectric. The resonant angle and resonant wavelength are quite sensitive to changes in the refractive index of the dielectric of the adjacent metal. Therefore, detecting resonance conditions helps to determine the refractive index change of the sensing medium [12].

Conventional sensing techniques have generally worked on studying surface plasmons excited at a single metal-layer-dielectric interface within SPR sensors based on Kretschmann structures. In recent years, several reports have proposed advanced structures supporting surface plasmon modes [13]. These structures typically apply more layers compared to conventional single-layer SRP structures. The utilization of more layers causes more degrees of freedom in the design, thus allowing the control of the SPR feature width [14], the penetration depth of the surface plasmon field into the medium, the optimization of the sensor sensitivity, and even the excitation of more surface plasma modes with different penetration depths [15]. In addition, there are many further analyses and studies, ranging from structural configurations, experimental setups, and applications to different phenomena, which have flourished in the field of sensing. In 2022, Pei et al. [16] theoretically studied the classical analogy of double EITs in a periodic array of metal nanodisks on a dielectric film. Zhang et al. [17] proposed an optical gas sensor based on the SPR of nanoporous gold (NPG) thin films. Comparison of the spectral sensitivity to 100 ppm H_2S indicated that the NPG-SPR sensor was at least 6 times more sensitive than a conventional Au-SPR sensor. Before this, Mohammad et al. [18] proposed and analysed an enhanced structure for a compact and high-sensitivity plasmonic refractive index sensor by coupling of two metal-insulator-metal (MIM) waveguides with a silver nanorod array embedded into a square resonator. The refractive index and temperature sensitivity values can be obtained as high as 2320 nm per refractive index unit and 0.84 nm/°C. Additionally, they presented a compact refractive index sensor in a two-dimensional plasmonic waveguide by hexagonal-ring cavity [19] and a high-sensitivity plasmonic sensor using three-dimensional plasmonic MIM waveguides and a racetrack resonator [20]. The refractive index sensitivity values could be obtained as high as 4270 nm per refractive index unit and 4650 nm per refractive index unit, respectively. For research based on MIM waveguide structures, Jian et al. [21] designed a structure coupled with symmetric T-type resonators, which achieved a maximum sensitivity of 1012 nm/RIU and a FOM of 5.57×10^4. Liu et al. [22] presented a refractive index sensor based on Fano resonance, which is generated by the coupling of a MIM waveguide structure and a toroidal cavity with a built-in elliptical ring structure. The structure has a maximum sensitivity of 2220 nm/RIU and a FOM of 58.7. As the analysis of this type of sensor is generally numerical, Muhammad analysed the feasibility of MIM-waveguide-based sensors [23]. Likewise, other configurations of the sensor yielded favourable results. Gavela et al. [24] reported on novel transducers and materials, improvements of existing transducers, new and improved biofunctionalization procedures, and the prospects for near future commercialization of these technologies. Alberto [25] presented an overview of the photonic-crystal-based biosensors for cancer biomarkers detection. Nabarun et al. [26] proposed a highly sensitive RI sensor based on a compact high-index-coated polymer waveguide Bragg grating with metal under the cladding. The structure has a sensitivity of 408–861 nm/RIU over a broad dynamic range of 1.32–1.44. Moreover, Butt et al. [27] presented a numerical study on the modified Bragg grating structure based on a MIM waveguide that could be simultaneously employed as an optical filter and temperature sensor. The modified Bragg grating structure could be simultaneously employed as a bandstop filter (bandwidth~200 nm) and temperature sensor with an attractive sensitivity of 0.47 nm/°C. In addition, a compact and ultra-high sensitive refractive index sensor based on modal interference in an integrated optic waveguide with a metal under-cladding was proposed by Ranjeet et al. [28]. The structure was found to vary in the range of 5.28–71.94 m/RIU for the RI range of 1.33–1.37, which is the highest reported RI

sensitivity achieved in modal-interference-based sensors to date. Zhe et al. [29] proposed a method for refractive index sensing based on surface plasmon coupled emission, consisting of a reverse Kretschmann or a Tamm structure for the first time. The corresponding sensing sensitivity reached 87.61 deg/RIU and 67.44 deg/RIU, respectively.

Furthermore, terahertz metamaterials are also a hot topic of research. Zhe et al. [30] fabricated a transmissive terahertz metamaterial using a folding metamaterial comprising split-ring resonators with nano-profiles with a high aspect ratio of 41.4. The folding metamaterial has a small transmittance of -49 dB at its resonance frequency, significant transmittance contrast of approximately 6×10^4 to the transmittance of its substrate, sizeable refractive index sensitivity of 647 GHz/RIU, and a large quality factor of 37. Harry et al. [31] proposed a simple method that is compatible with all geometrical structures of terahertz metamaterials to increase their refractive index sensitivities. This method used a patterned photoresist to float the split-ring resonators (SRRS) of a terahertz metamaterial at the height of 30 µm from its substrate deposited with complementary SRRs. The floating terahertz metamaterial has a considerable refractive index sensitivity of 532 GHz/RIU because its near field is not distributed over the substrate, and the complementary SRRs confine the field above the substrate. Additionally, Yin et al. [32] reported a magnetic-free THz unidirectional perfect absorber and a functionality-switchable device between the band-pass filter and perfect absorber based on dielectric graphene multilayers containing a VO_2 defect layer.

In addition to the structural configurations described above, another structure that consists of two metallic layers with similar refractive indices, namely the insulator-metal-insulator structure. When the film is thin enough, the plasmon-polariton modes guided by the interfaces become coupled due to field tunnelling through the metal, thus creating supermodes that exhibit a dispersion varying with metal thickness [33]. Surface plasma waves propagating on the surface of the metal layers start coupling when they have similar propagation constants, leading to the formation of two new modes, the low-loss long-range surface plasma (LRSPP) and the high-loss short-range surface plasma (SRSPP), respectively, where LRSPP is also called symmetric mode, and SRSPP is called antisymmetric mode. [34] These two coupling modes can be excited in the Kretschmann geometry. In optical sensing, LRSPP receives more attention compared to conventional SRP because LRSPP can produce narrower SPR characteristic curves, lower losses, and longer propagation distances. A higher local field strength and a relatively long propagation distance are incompatible with the traditional SPR sensor structure. Therefore, the IMI-based sensor design proposed in this work is capable of having a longer detection length and better sensitivity by generating LRSPP. The materials are more readily available and can provide a more convenient reference for preparing subsequent structures.

2. Theoretical Models and Numerical Methods

Figure 1 shows the proposed structure. The incident light is a TM wave, the incident wavelength sets to 816 nm, and the incident angle is 63.1°. In the composition of the structure, the sensing medium, Au, Al_2O_3, Au, MgF_2, and BK7 prism, are in order from top to bottom. On the upper side of the sensing medium is air. The first IMI structure comprises three layers: MgF_2, Au, and Al_2O_3; the second IMI structure is composed of Al_2O_3, Au, and the sensing medium. When these two structures satisfy the wave vector matching condition, the SPW generated at the MgF_2–Au interface, the Au–Al_2O_3 interface, the Al_2O_3–Au interface and the Au–sensing medium interface will couple. The modes generated by these two structures result in a decrease in the field intensity distribution inside the two metal layers and an increase in the field intensity distribution in the dielectric layer. At this point, the sensitivity of the sensor will increase with the enhancement of the field strength in the sensing medium layer.

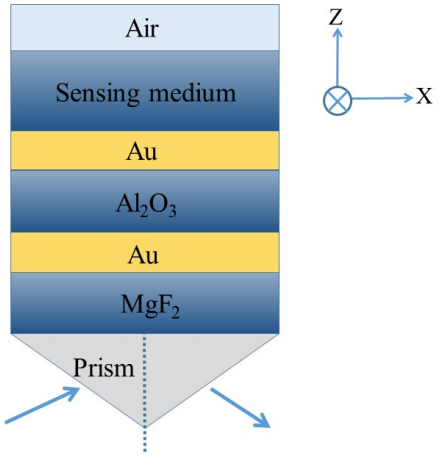

Figure 1. Schematic diagram of proposed structure.

In this structure, the refractive index of the BK7 prism is given by the following expression [35]:

$$n_{BK7} = \left(\frac{1.03961212\lambda^2}{\lambda^2 - 0.00600069867} + \frac{0.231792344\lambda^2}{\lambda^2 - 0.0200179144} + \frac{1.03961212\lambda^2}{\lambda^2 - 103.560653} + 1\right)^{1/2} \quad (1)$$

The refractive index of the second layer medium MgF_2 is given by the following expression (from https://refractiveindex.info/, accessed on 8 January 2023):

$$n_{MgF_2} = \left(\frac{0.48755108\lambda^2}{\lambda^2 - 0.4338408^2} + \frac{0.39875031\lambda^2}{\lambda^2 - 0.09461442^2} + \frac{2.3120353\lambda^2}{\lambda^2 - 23.793604^2} + 1\right)^{1/2} \quad (2)$$

Since the conventional Drude model fails in both the visible and UV regions [36]. The Drude-Lorentz model is an improvement on the Drude model. It is able to be implemented on various semiconductors and metals [37] and is compatible with the finite difference time domain method (FDTD), making it suitable for simulation of optical devices [38]. We generally use this model to calculate the dielectric constant of metals. The third and fifth layers are gold films, whose dielectric constants are expressed by the Drude-Lorentz mode [39]:

$$\varepsilon_m = 1 - \frac{\lambda^2 \lambda_c}{\lambda_p^2(\lambda_c + i\lambda)}, \quad (3)$$

where is the incident wavelength; λ_c is the collision wavelength of the metal with a value of 8.9342×10^{-6} m; and λ_p is the plasma wavelength of the metal with a value of 1.6826×10^{-7} m [40].

The fourth layer is the Al_2O_3 film, which has the refractive index, as shown in the following expression (from https://refractiveindex.info/, accessed on 8 January 2023):

$$n_{Al_2O_3} = \left(\frac{1.4313493\lambda^2}{\lambda^2 - 0.0726631^2} + \frac{0.65054713\lambda^2}{\lambda^2 - 0.1193242^2} + \frac{5.3414021\lambda^2}{\lambda^2 - 18.028251^2} + 1\right)^{1/2} \quad (4)$$

Figure 2 shows the diagrams of these two IMI structures, in which the thickness of MgF_2 (d_1) and Al_2O_3 (d_3) are set to 50 nm, and the thickness of the sensing dielectric layer (d_5) is set to 4800 nm. Then, the dispersion equation is needed to calculate the thickness of the two gold films in the structure corresponding to d_2 and d_4, respectively. The dielectric constants of each layer of the dielectric layer from the bottom to the top are set as ε_1, ε_2, ε_3, ε_4, and ε_5. The thickness of each layer is d_1, d_2, d_3, d_4, and d_5.

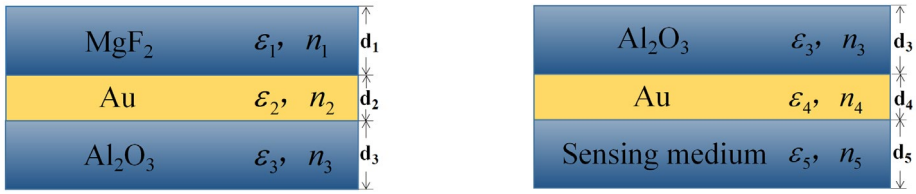

Figure 2. (**a**) Schematic diagrams of the first IMI structure; (**b**) Schematic diagrams of the second IMI structure.

From the boundary continuity of the electric and magnetic fields, the dispersion equation of the IMI structure can be solved. By Figure 2a,b, the dispersion equation of the first IMI structure is formulated by the following two expressions [41]:

$$e^{-4k_2 \cdot d_2/2} = \frac{k_2/\varepsilon_2 + k_3/\varepsilon_3}{k_2/\varepsilon_2 - k_3/\varepsilon_3} \cdot \frac{k_2/\varepsilon_2 + k_1/\varepsilon_1}{k_2/\varepsilon_2 - k_1/\varepsilon_1} \tag{5}$$

$$e^{-4k_4 \cdot d_4/2} = \frac{k_4/\varepsilon_4 + k_5/\varepsilon_5}{k_4/\varepsilon_4 - k_5/\varepsilon_5} \cdot \frac{k_4/\varepsilon_4 + k_3/\varepsilon_3}{k_4/\varepsilon_4 - k_3/\varepsilon_3} \tag{6}$$

In Formulas (5) and (6), the wave vector in each layer of the medium is denoted by k_j, where j can be taken from 1 to 5. It is related to the propagation constant (β_i) of the modes by the following equation:

$$k_j^2 = {\beta_i}^2 - k_0^2 \varepsilon_j \tag{7}$$

When the effective indices of these two modes match, these two modes will couple together to produce a greater field intensity to achieve our optimization purpose. The effective refractive index can be calculated by the following equation:

$$n_{effi} = \frac{\beta_i}{k_0} \tag{8}$$

In Formulas (7) and (8), the letter i can be taken as 1 or 2, indicating the propagation constants of the two IMI structures, respectively. Additionally, k_0 represents the wave vector in vacuum. Therefore, the thickness of the two metal layers can be analysed and calculated by the effective refractive index. Due to the complexity of the calculations, we use Boundary Modal Analysis of COMSOL software to assist in the calculations. The effective refractive index of the overall structure is 1.3474. The thicknesses of the two metal layers, d_2 and d_4, can be acquired by the relational equation of the effective refractive index according to the dispersion relationship. From Figure 3, it can be seen that when the effective refraction is 1.3474, the thicknesses of the 2 gold layers are 18.8 nm and 20 nm, respectively.

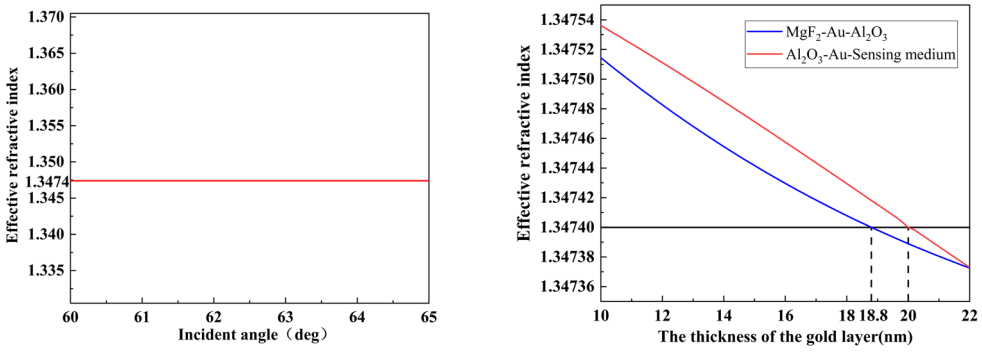

Figure 3. (**a**) Effective refraction of the overall structure; (**b**) Relationship between metal thickness and effective refractive index in two structures.

The transmission matrix method (TMM) and the Fresnel equation based on the N-layer model are used to analyse the reflectivity of multilayer systems [42,43]. Each layer of the multilayer structure can be expressed as a matrix:

$$M_k = \begin{bmatrix} \cos\beta_k & (-i\sin\beta_k)/q_k \\ -iq_k\sin\beta_k & \cos\beta_k \end{bmatrix}, \quad (9)$$

where

$$\beta_k = \frac{2d_k\pi}{\lambda}(\varepsilon_k - n_1^2\sin^2\theta)^{1/2} \quad (10)$$

and

$$q_k = \frac{(\varepsilon_k - n_1^2\sin^2\theta)^{1/2}}{\varepsilon_k}. \quad (11)$$

Here, d_k is the thickness of each layer in the multilayer sensing structure, ε_k is the dielectric constant of each layer, and n_1 is the RI of the prism. The characteristic transfer matrix of the sensing configuration is as follows:

$$M = \prod_{k=2}^{N-1} M_k = \begin{bmatrix} M_{11} & M_{12} \\ M_{21} & M_{22} \end{bmatrix}. \quad (12)$$

The reflectivity of the multi-layer sensing structure is shown in the following equation:

$$R = |r_p|^2 = \left| \frac{(M_{11} + M_{12}q_N)q_1 - (M_{21} + M_{22}q_N)}{(M_{11} + M_{12}q_N)q_1 + (M_{21} + M_{22}q_N)} \right|^2. \quad (13)$$

The parameters of SPR sensors, such as sensitivity and figure of merit, can be used to evaluate the performance of the sensor. Since this research focuses on wavelength modulation, the corresponding sensitivity is defined as the ratio of the displacement ($\Delta\lambda$) of the resonance wavelength to the change in the refractive index (Δn_s) of the sensing medium, and the expression is as follows:

$$S = \frac{\Delta\lambda}{\Delta n_s}. \quad (14)$$

Another performance metric, FOM, is defined by the expression:

$$FOM = \frac{S}{FWHM}, \quad (15)$$

where FWHM is full width at half maximum, corresponding to half the width of the resonance peak.

3. Experimental Results and Analysis

3.1. Influence of Metal Layer Thickness

Compared to other metals, gold exhibits a farther resonance parameter shift associated with RI changes in the sensing layer [39]. Moreover, gold is chemically stable and is not easily oxidized. Therefore, gold is chosen as the preferred metal in this work. According to the effective refractive index results in Figure 3b, the 2 modes are coupled when the thicknesses of the first metal layer and the second metal are 18.8 nm and 20 nm, respectively. To verify this result, two different sets of metal layer thicknesses were selected for experiments. The experimental results are shown in Figures 4 and 5.

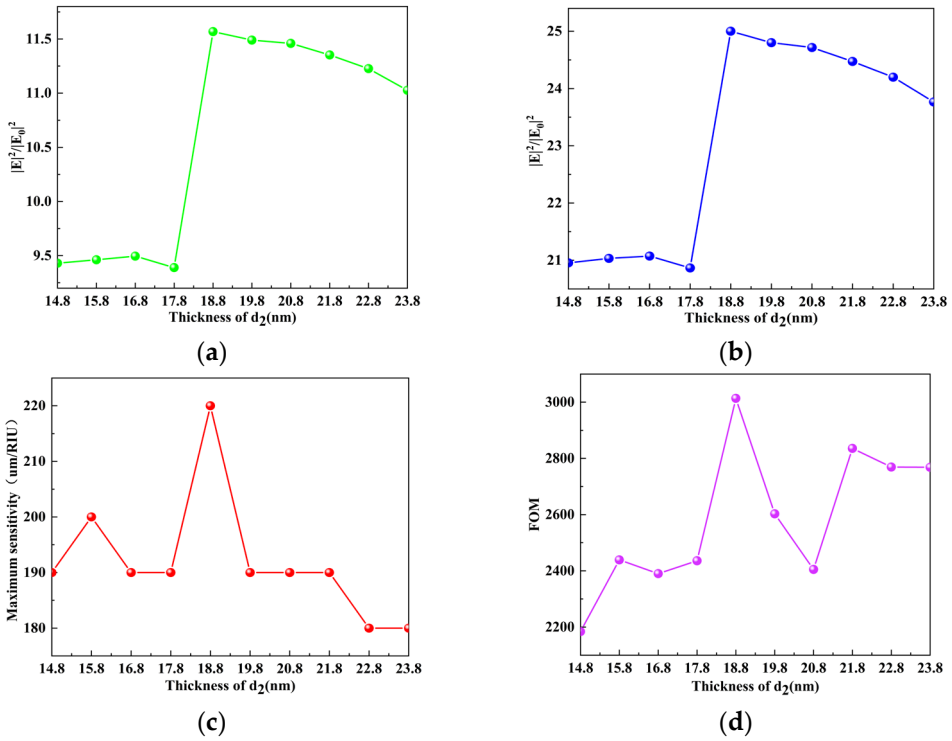

Figure 4. Under the conditions of different thicknesses of the first gold layer, the electric field mode (**a**) at the metal-sensing dielectric layer interface and (**b**) in the middle of the sensing dielectric layer, (**c**) maximum wavelength sensitivity of the structure, and (**d**) FOM.

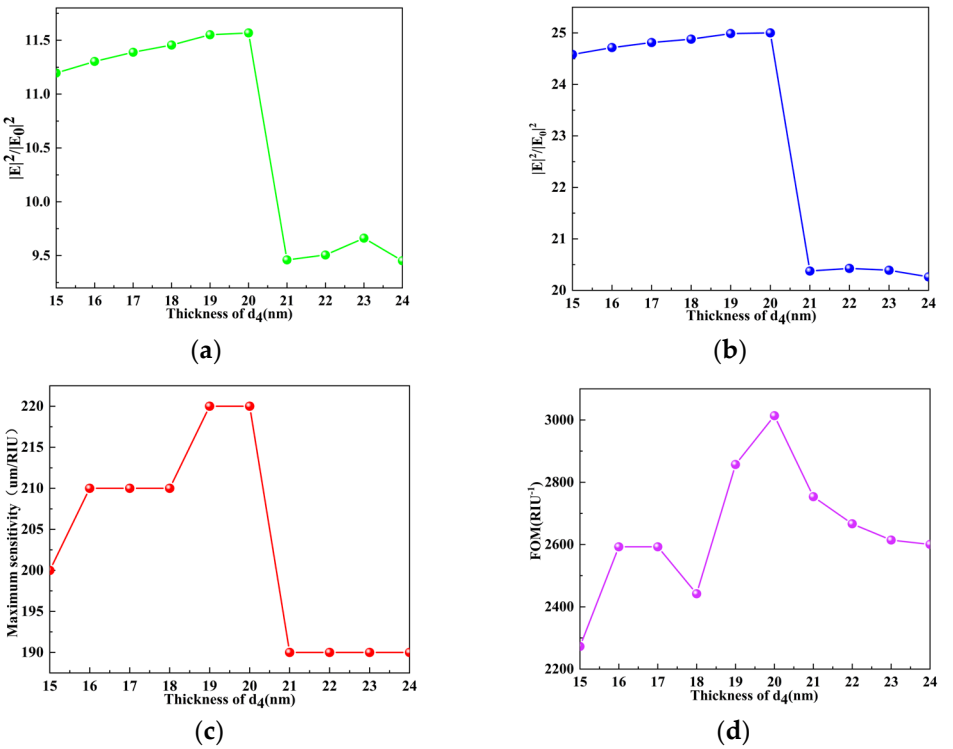

Figure 5. Under the conditions of different thicknesses of the second gold layer, the electric field mode (**a**) at the metal-sensing dielectric layer interface and (**b**) in the middle of the sensing dielectric layer, (**c**) maximum wavelength sensitivity of the structure, and (**d**) FOM.

3.2. The Choice of Dielectric Layer and the Impact of Different Dielectric Layers

MgF_2 is a stable optical coating material that can be widely used in the design and development of various optical coatings. It is also a low refractive index material, similar to the refractive index of the analyte. Similar to MgF_2, LiF has a comparable refractive index to the analyte. The refractive index of the sensing medium(n_s) varies in the range of 1.3494–1.3500, and the dielectric material of the second layer is Al_2O_3. When the first dielectric layer is MgF_2 and LiF, respectively, the sensitivity and FOM obtained by the model are shown in Figure 6a,b. As seen from the figures, the sensitivity decreases with the increase in the ns. When the first dielectric layer is LiF, the maximum sensitivity (S_{max}) is 200 μm/RIU, and the corresponding FOM is 2816.90 RIU^{-1}. By the time the dielectric layer is MgF_2, the S_{max} is 220 μm/RIU, and the corresponding FOM is 3013.70 RIU^{-1}. The maximum sensitivity and FOM acquired for MgF_2 in this range are above those for LiF. In this work, consequently, MgF_2 is adopted as the first dielectric layer.

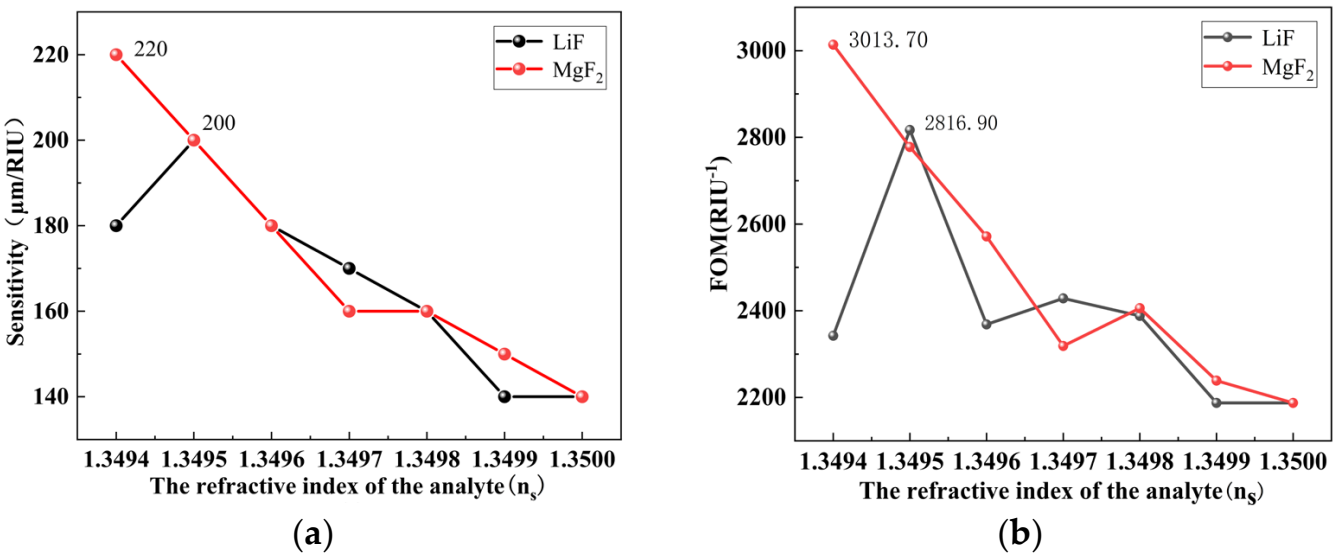

Figure 6. (**a**) Sensitivity obtained when the first dielectric layer is MgF_2 and LiF, respectively. (**b**) FOM obtained when the first dielectric layer is MgF_2 and LiF, respectively.

For oxides, usually, the imaginary part of the refractive index is negligible. When highly refractive oxides are combined with Au, the performance of the sensor is improved [44]. The first dielectric layer is MgF_2; comparison of the performance of the sensor in the refractive index range of 1.3494 to 1.3500 for the analytes on the second dielectric layer for Al_2O_3, SiO_2, MgO, and TiO_2, respectively, is shown in Table 1. According to Table 1, the sensitivity tends to decline with the rise in RI of the measured medium for all four materials. The S_{max} of the sensor with Al_2O_3 is 220 μm/RIU, and the average sensitivity is 172.86 μm/RIU, which is higher than the sensitivity and average sensitivity of the other 3 materials with the corresponding sensors. The corresponding maximum FOM and average FOM are also the highest with 3013.70 RIU^{-1} and 2502.01 RIU^{-1}, respectively. It is clear from Table 1 that when the second dielectric layer is Al_2O_3, the performance of the structure is better than those of the other three oxides. Moreover, Al_2O_3 is simpler to acquire and more chemically stable, with robust light transmission and adsorption ability. Therefore, in selecting of the second layer of the medium, Al_2O_3 is preferred.

Table 1. Sensitivity, average sensitivity, FOM, and average FOM obtained for four different media in the RI variation range of 1.3494–1.3500.

Oxide	RI	S (μm/RIU)	Average S (μm/RIU)	FOM (RIU^{-1})	Average FOM (RIU^{-1})
SiO_2	1.3494	180	171.43	2037.69	2443.73
	1.3495	200		2857.14	
	1.3496	200		2898.55	
	1.3497	160		2381.84	
	1.3498	160		2253.52	
	1.3499	160		2253.52	
	1.3500	140		2153.85	
MgO	1.3494	180	171.43	1689.11	2324.09
	1.3495	200		2777.78	
	1.3496	200		2777.78	
	1.3497	160		2222.22	
	1.3498	160		2285.94	
	1.3499	160		2352.94	
	1.3500	140		2153.85	
TiO_2	1.3494	200	162.86	2985.07	2455.60
	1.3495	200		3030.30	
	1.3496	160		2388.06	
	1.3497	160		2153.85	
	1.3498	140		2187.50	
	1.3499	140		2222.22	
	1.3500	140		2222.22	
Al_2O_3	1.3494	220	172.86	3013.70	2502.01
	1.3495	200		2777.78	
	1.3496	180		2571.49	
	1.3497	160		2318.84	
	1.3498	160		2406.02	
	1.3499	150		2238.50	
	1.3500	140		2187.50	

3.3. Effect of Different Numbers of Layers on Sensor Performance

To explore whether different numbers of layers have an impact on the performance of this structure, the performance of sensors with different numbers of layers is contrasted within a variation of the analyte refractive index of 1.3494–1.3500 under the same materials and thickness. The contrasted sensors include the long-range surface plasmon resonance (LPSPR) sensor (consisting of BK7 prism, MgF_2, Au, and sensing medium), the first IMI-type sensor (consisting of BK7 prism, MgF_2, Au, Al_2O_3, and sensing medium), the second IMI-type sensor (consisting of BK7 prism, Al_2O_3, Au, and sensing medium, where the Al_2O_3, Au, and sensing medium layers form the IMI structure), and the proposed sensor. As seen from Figure 7a, although the sensitivity of all 4 structures decreases, the sensitivity of the proposed structure is superior to the other 3 types of sensors in the range of 1.3494–1.3496 refractive index of the analyte. With the increasing refractive index of the analyte, the sensitivity of several structures is similar. It can be seen from Figure 7b that, like the sensitivity, the FOM also decreases gradually with the increase in the refractive index of the sensing medium layer. The figure of merit of the proposed sensor is about four times that of the LRSRP sensor and three times that of the first and second IMI sensors. Consequently, the overall performance of the proposed structure is higher than the sensing performances of the other three structures.

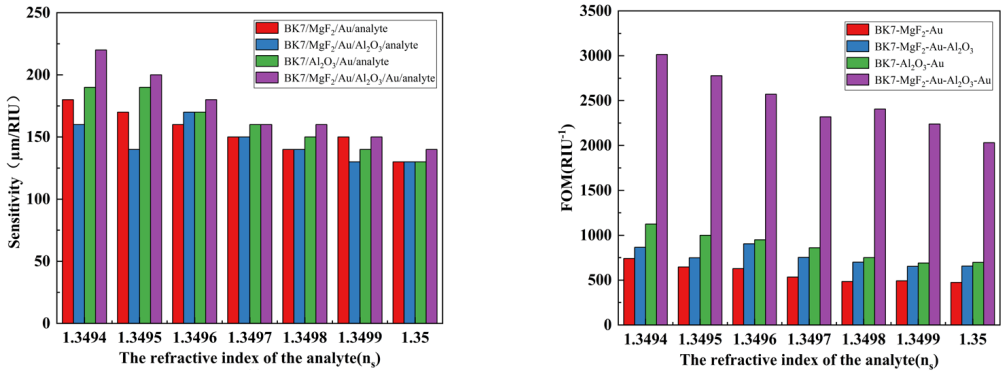

Figure 7. (**a**) Sensitivity obtained for sensors with different types of structures in the refractive index range of 1.3494–1.3500; (**b**) FOM obtained for sensors with different types of structures in the refractive index range 1.3494–1.3500.

3.4. Sensor Based on IMI Structure

From Figure 3a, it can be seen that the effective refractive index of the incident angle from 60 degrees to 65 degrees is 1.3474. Under the condition that the incident angle is 63.1° and the incident light is a TM wave, Figure 8a,b show that the mode field inside the 2 layers of metal is tiny. The magnetic field intensity is only slightly attenuated near the centre of the metal and does not reach zero or a negative value. In both structures, the magnetic field intensity in the Z-direction generated at the gold–dielectric interface farther away from the prism is higher than that at the gold–dielectric partition interface closer to the prism, which means that the LRSPP of both IMI structures are excited [45]. At this time, the excited long-range surface plasmon wave (LRSPW) will be coupled when the matching condition is satisfied so that the field at the metal-sensing medium surface is enhanced. LRSPW has a long propagation distance. Additionally, the light wave will be reflected when propagating from one medium to another. Consequently, the LRSPW propagating from the metal-sensing medium interface will be coupled with the LRSPW reflected back from the sensing medium–air interface when the wave vector matching condition is satisfied. As seen from Figure 9a–d, the electromagnetic field distribution of the proposed structure is approximately the same as in the BK7/Al_2O_3/Au/analyte structure. In this case, standing waves are generated. However, the FWHM of the BK7/Al_2O_3/Au/analyte structure needs to be narrower, resulting in a lower FOM than that of the proposed structure, as shown in Figure 7b. At this time, the electric field strength in the sensing medium is powerful, about two folds of the field strength attained by the gold-sensing medium interface, as shown in Figure 10. The proposed sensor achieved a more desirable sensitivity due to the secondary enhancement of the field strength.

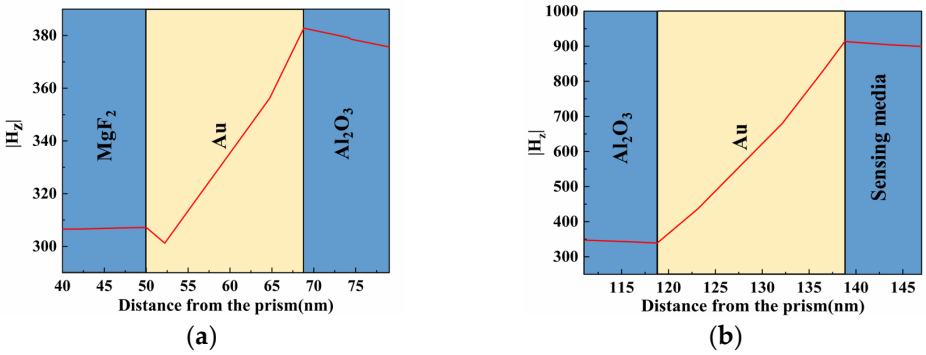

Figure 8. (**a**) Magnetic field mode distribution in the Z-direction for the first IMI structure; (**b**) Magnetic field mode distribution in the Z-direction for the second IMI structure.

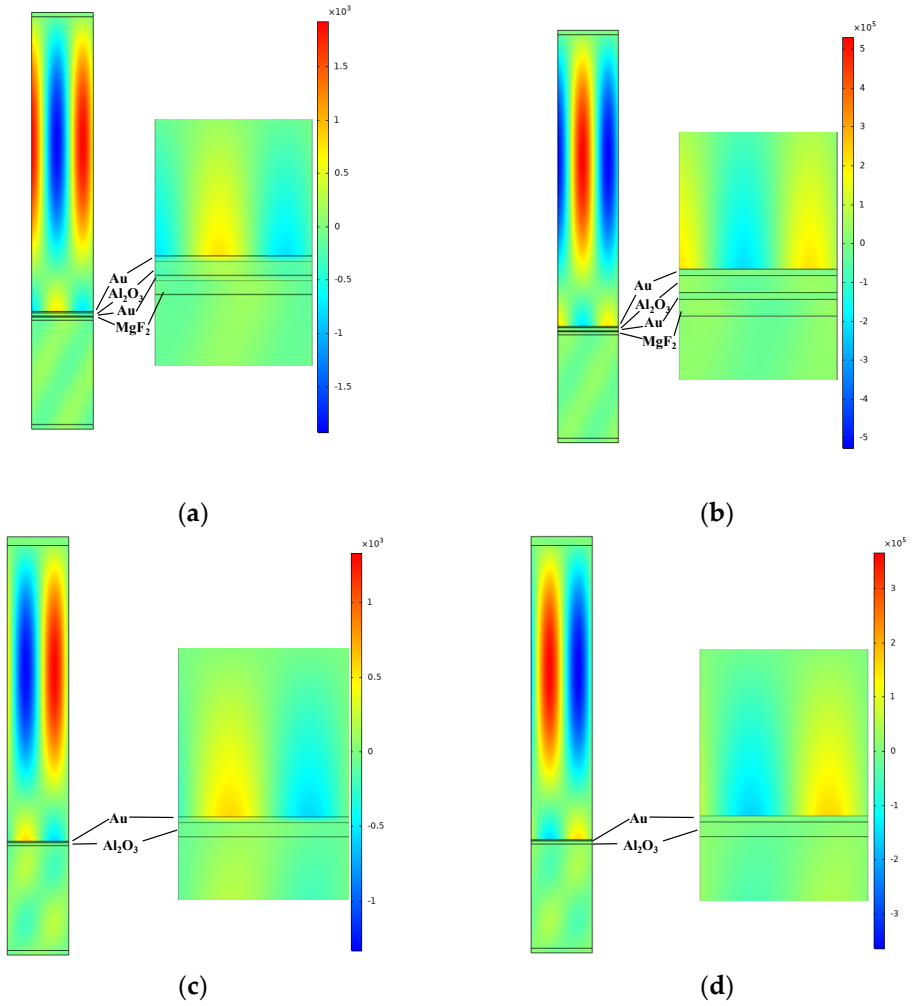

Figure 9. (**a**) Magnetic field component in the Z-direction in the BK7/MgF_2/Au/Al_2O_3/A u/analyte structure; (**b**) Electric field component in the Y-direction in the BK7/MgF_2/Au/Al_2O_3/Au/analyte structure; (**c**) Magnetic field component in the Z-direction in the BK7/Al_2O_3/Au/analyte structure; (**d**) Electric field compone nt in the Y-direction in the BK7/Al_2O_3/Au/analyte structure.

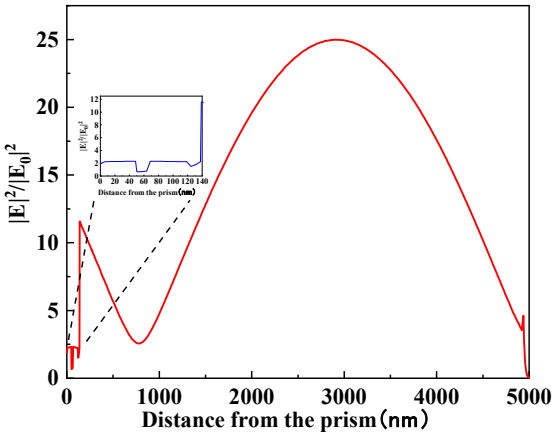

Figure 10. Electric field mode distribution of the proposed structure.

Figure 11a shows the results of wavelength modulation for this structure in the analyte variation range of 1.3494–1.3507, where the refractive index of the medium to be measured changes by 0.0001. Ten sets of data are taken from this and plotted. The relationship is fitted to express the trend of resonance wavelength variation with analyte

RI, as shown in Figure 11b. While the refractive index was varied from 1.3494–1.3504, the optimal resonance wavelength shift is 22 nm, the wavelength sensitivity is 220 µm/RIU, the full width at half maximum is 73 nm, the FOM is 3013.70 RIU^{-1}, and the average wavelength sensitivity is 156.36 µm/RIU. Typical analytes that can be detected in this range are glycerol at low concentrations in deionised water [46], haemoglobin at around 150 g/l [47], and glucose solutions at around 15% mass fraction [48]. According to this current study on SPR, the comparison of wavelength sensitivity and figure of merit are shown in Table 2. Two different structures obtained a higher sensitivity of 330 µm/RIU [49] and 400 µm/RIU [50], respectively. The former sensor structure was based on metamaterials and obtains a better sensitivity. However, its FOM was not ideal. The FOM of the structure proposed in this paper is about six times higher. The latter proposed sensor was based on optical fibres and also achieved a relatively high sensitivity. Yet, its detection range is too narrow, being limited to the refractive index variation in the range of 1.33–1.3382. The structure proposed in this paper is capable of adjusting the RI detection range and operating wavelength of the analyte according to the angle of incidence. For example, when the angle of incidence is fixed at 60°, the proposed structure can operate in the refractive index range of 1.33–1.45, and the operating wavelength is 700–1950 nm. In this range, the sensitivity, FOM and electric field modes generated by wavelength modulation are shown in Figure 12. In summary, the overall performance of the structure proposed in this work has achieved favourable results.

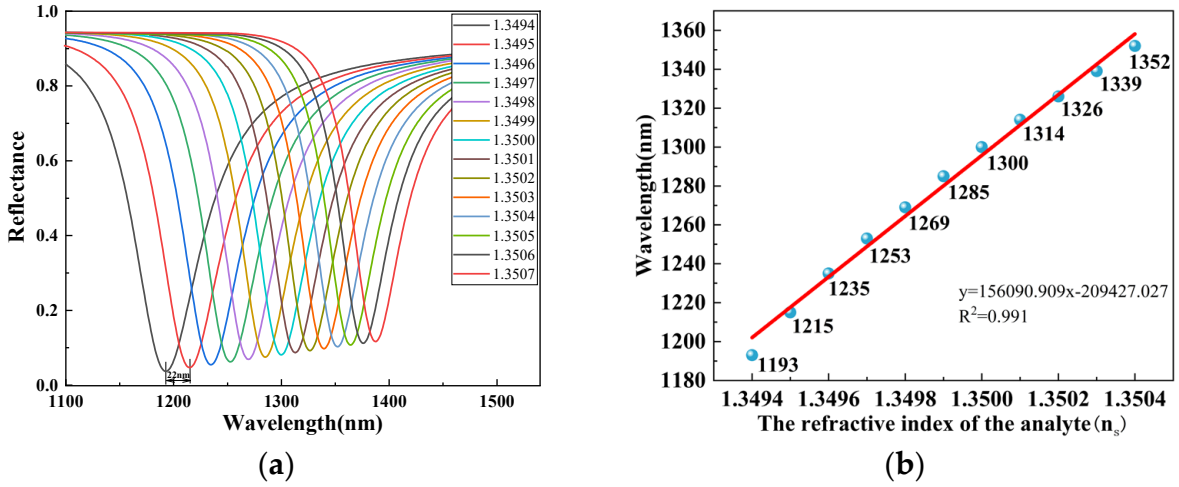

Figure 11. (**a**) Plot of wavelength modulation results in the refractive index range of 1.3494–1.3507; (**b**) Linear fit of the sensitivity of the proposed structure.

Table 2. Comparison of performance parameters of different sensor structures under wavelength modulation.

Configuration	Operating Wavelength (nm)	RI Range	S (µm/RIU)	FOM (RIU^{-1})	Reference
BK7/Teflon/Au/analyte	-	1.330–1.355	59	1552.63	[51]
BK7/Cr/Au/GeSe/analyte	400–1000	1.33–1.36	3.58	14.37	[52]
SF14/Teflon/Au/analyte	500–800	1.334–1.337	38	-	[10]
Fibre core-MgF_2/Au/MgF_2/analyte	550–750	1.33–1.38	5.28	156.19	[12]
BAF10/Cytop/ZnO/Au/ZnO/analyte	580–730	1.333–1.334	60	1857	[53]
SF10/Cytop/$CH_3NH_3PbBr_3$/Au/analyte	620–660	1.33–1.34	7.29	1240	
HMM-Au Grating/analyte	1200–1400	1.3333–1.3336	30	590	[11]
HMM-Prism Ag/analyte	1400–2526	1.33–1.334	330	492	[49]
Fibre/Cu/analyte	750–2700	1.33–1.3382	400	-	[50]
BK7-MgF_2-Au-Al_2O_3-Au/analyte	700–1950	1.3494–1.3507	220	3013.70	This paper

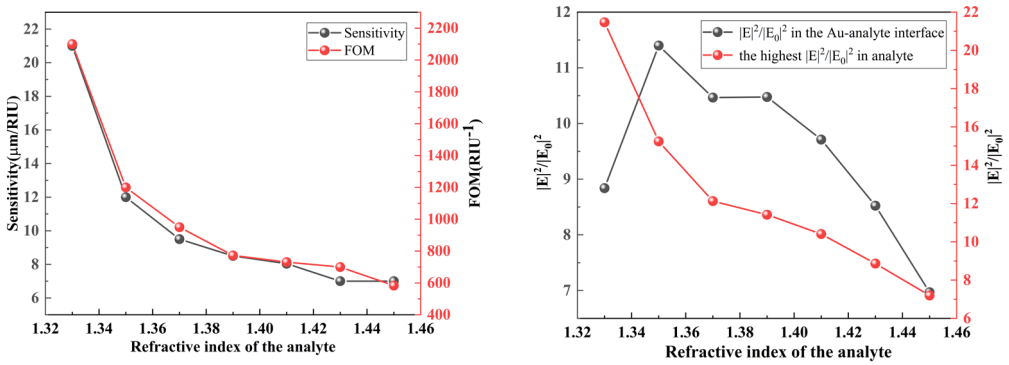

Figure 12. (**a**) The sensitivity and FOM achieved by wavelength modulation of the sensor at an incidence angle of 60° and a RI range of 1.33–1.45; (**b**) The electric field mode of this structure at the Au-analyte interface and inside the analyte at 60°.

4. Conclusions

In this work, a combination of $MgF_2/Au/Al_2O_3$ and Al_2O_3/Au/sensing medium was used to constitute the proposed IMI-structure-based sensor. From the analysis of the electromagnetic field intensity distribution, it is found that the structure can excite symmetrical modes. The generation of LRSPP provides the sensor with enhanced field strength. Meanwhile, the impact of the thickness of the metal layer, the choice of the dielectric layer material, and the number of structural layers on the performance of the model were discussed. In a refractive index range of 1.3494–1.3504, the highest sensitivity of the optimized sensor by wavelength modulation is 220 μm/RIU, the figure of merit is 3013.70 RIU^{-1}, and the average sensitivity is 156.36 μm/RIU. As the results indicate, the presented sensor is sensitive to slight variations of refractive index. The achieved sensitivity is about an order of magnitude higher than that of conventional SPR sensors. In addition, the measuring range and operating wavelength of the sensor could be adjusted by changing the angle of incidence. Therefore, the proposed sensor is considered to have potential applications in the field of biosensing.

Author Contributions: Conceptualization, X.C. and Z.G.; software, X.C. and Z.L.; validation, X.C.; data curation, X.C.; writing—original draft preparation, X.C.; writing—review and editing, X.C., Z.G., Z.L., J.W., H.W. and S.C.; supervision, J.S. and C.L.; funding acquisition, J.S. and C.L. All authors have read and agreed to the published version of the manuscript.

Funding: This work was funded by Finance Science and Technology Project of Hainan Province (ZDKJ2020009).

Institutional Review Board Statement: Not applicable.

Informed Consent Statement: Not applicable.

Data Availability Statement: Research data presented in this study are available on request from the corresponding author.

Conflicts of Interest: The authors declare no conflict of interest.

References

1. Berini, P. Plasmon-polariton waves guided by thin lossy metal films of finite width: Bound modes of symmetric structures. *Phys. Rev. B* **2000**, *61*, 10484–10503. [CrossRef]
2. Fan, Y.-E.; Zhu, T.; Shi, L.; Rao, Y.-J. Highly sensitive refractive index sensor based on two cascaded special long-period fiber gratings with rotary refractive index modulation. *Appl. Opt.* **2011**, *50*, 4604–4610. [CrossRef] [PubMed]
3. Miroshnichenko, A.E.; Flach, S.; Kivshar, Y.S. Fano resonances in nanoscale structures. *Rev. Mod. Phys.* **2010**, *82*, 2257–2298. [CrossRef]
4. Nenninger, G.; Tobiška, P.; Homola, J.; Yee, S. Long-range surface plasmons for high-resolution surface plasmon resonance sensors. *Sens. Actuators B Chem.* **2001**, *74*, 145–151. [CrossRef]

5. Wood, R.W. On a remarkable case of uneven distribution of light in a diffraction grating spectrum. *Lond. Edinb. Dublin Philos. Mag. J. Sci.* **1902**, *4*, 396–402. [CrossRef]
6. Liedberg, B.; Nylander, C.; Lunström, I. Surface plasmon resonance for gas detection and biosensing. *Sens. Actuators* **1983**, *4*, 299–304. [CrossRef]
7. Homola, J. Surface plasmon resonance sensors for detection of chemical and biological species. *Chem. Rev.* **2008**, *108*, 462–493. [CrossRef]
8. Piliarik, M.; Párová, L.; Homola, J. High-throughput SPR sensor for food safety. *Biosens. Bioelectron.* **2009**, *24*, 1399–1404. [CrossRef]
9. Šípová, H.; Homola, J. Surface plasmon resonance sensing of nucleic acids: A review. *Anal. Chim. Acta* **2013**, *773*, 9–23. [CrossRef]
10. Sreekanth, K.V.; Alapan, Y.; ElKabbash, M.; Ilker, E.; Hinczewski, M.; Gurkan, U.A.; De Luca, A.; Strangi, G. Extreme sensitivity biosensing platform based on hyperbolic metamaterials. *Nat. Mater.* **2016**, *15*, 621–627. [CrossRef]
11. Feng, X.; Yang, M.; Luo, Y.; Tang, J.; Guan, H.; Fang, J.; Lu, H.; Yu, J.; Zhang, J.; Chen, Z.J.O.; et al. Long range surface plas-mon resonance sensor based on side polished fiber with the buffer layer of magnesium fluoride. *Opt. Quantum Electron.* **2017**, *49*, 1–12. [CrossRef]
12. Shukla, S.; Sharma, N.K.; Sajal, V. Sensitivity enhancement of a surface plasmon resonance based fiber optic sensor using ZnO thin film: A theoretical study. *Sens. Actuators B Chem.* **2015**, *206*, 463–470. [CrossRef]
13. Slavík, R.; Homola, J. Optical multilayers for LED-based surface plasmon resonance sensors. *Appl. Opt.* **2006**, *45*, 3752–3759. [CrossRef] [PubMed]
14. Chien, F.-C.; Chen, S.-J. Direct determination of the refractive index and thickness of a biolayer based on coupled waveguide-surface plasmon resonance mode. *Opt. Lett.* **2006**, *31*, 187–189. [CrossRef] [PubMed]
15. Matsubara, K.; Kawata, S.; Minami, S. Multilayer system for a high-precision surface plasmon resonance sensor. *Opt. Lett.* **1990**, *15*, 75–77. [CrossRef]
16. Huang, P.; Yao, Y.; Zhong, W.; Gu, P.; Yan, Z.; Liu, F.; Yan, B.; Tang, C.; Chen, J.; Zhu, M. Optical sensing based on classical analogy of double Electromagnetically induced transparencies. *Res. Phys.* **2022**, *39*, 105732. [CrossRef]
17. Zhang, C.; Liu, Z.; Cai, C.; Yang, Z.; Qi, Z.-M. Surface plasmon resonance gas sensor with a nanoporous gold film. *Opt. Lett.* **2022**, *47*, 4155. [CrossRef]
18. Rakhshani, M.R.; Mansouri-Birjandi, M.A.J.S. High sensitivity plasmonic refractive index sensing and its application for human blood group identification. *Sens. Actuators B Chem.* **2017**, *249*, 168–176. [CrossRef]
19. Rakhshani, M.R.; Mansouri-Birjandi, M. High-sensitivity plasmonic sensor based on metal–insulator–metal wave-guide and hexagonal-ring cavity. *IEEE Sens. J.* **2016**, *16*, 3041–3046. [CrossRef]
20. Rakhshani, M.R.; Mansouri-Birjandi, M. Nanostructures-Fundamentals; Applications. A high-sensitivity sensor based on three-dimensional metal–insulator–metal racetrack resonator and application for hemoglobin detection. *Photonics Nanostructures Fundam. Appl.* **2018**, *32*, 28–34. [CrossRef]
21. Zhang, J.; Wang, X.; Zhu, J.; Chen, T.; Zhang, L.; Yang, H.; Tang, C.; Qi, Y.; Yu, J. Metal–insulator–metal waveguide structure coupled with T-type and ring resonators for independent and tunable multiple Fano resonance and refractive in-dex sensing. *Opt. Commun.* **2023**, *528*, 128993. [CrossRef]
22. Liu, F.; Yan, S.; Shen, L.; Liu, P.; Chen, L.; Zhang, X.; Liu, G.; Liu, J.; Li, T.; Ren, Y. A nanoscale sensor based on a toroidal cavity with a built-in elliptical ring structure for temperature sensing application. *Nanomaterials* **2022**, *12*, 3396. [CrossRef]
23. Butt, M. Metal-insulator-metal waveguide-based plasmonic sensors: Fantasy or truth—A critical review. *Appl. Res.* **2022**, e202200099. [CrossRef]
24. Gavela, A.F.; García, D.G.; Ramirez, J.C.; Lechuga, L.M. Last advances in silicon-based optical biosensors. *Sensors* **2016**, *16*, 285. [CrossRef]
25. Sinibaldi, A. Cancer biomarker detection with photonic crystals-based biosensors: An overview. *J. Light. Technol.* **2021**, *39*, 3871–3881. [CrossRef]
26. Saha, N.; Brunetti, G.; Kumar, A.; Armenise, M.N.; Ciminelli, C.J. Highly sensitive refractive index sensor based on poly-mer bragg grating: A case study on extracellular vesicles detection. *Biosensors* **2022**, *12*, 415. [CrossRef]
27. Butt, M.; Khonina, S.; Kazanskiy, N.J. A compact design of a modified Bragg grating filter based on a metal-insulator-metal waveguide for filtering and temperature sensing applications. *Optik* **2022**, *251*, 168466. [CrossRef]
28. Dwivedi, R.; Kumar, A. A compact and ultra high sensitive RI sensor using modal interference in an in-tegrated optic waveguide with metal under-cladding. *Sens. Actuators B Chem.* **2017**, *240*, 1302–1307. [CrossRef]
29. Shen, Z.; Hongda, Y.; Zhang, L.; Chen, Y. Refractive index sensing based on surface plasmon-coupled emission excited by reverse Kretschmann or Tamm structure. *Opt. Lett.* **2022**, *47*, 5068–5071. [CrossRef]
30. Silalahi, H.M.; Chiang, W.-F.; Shih, Y.-H.; Wei, W.-Y.; Su, J.-Y.; Huang, C.-Y. Folding metamaterials with extremely strong electromagnetic resonance. *Photon- Res.* **2022**, *10*, 2215. [CrossRef]
31. Silalahi, H.M.; Chen, Y.-P.; Shih, Y.-H.; Chen, Y.-S.; Lin, X.-Y.; Liu, J.-H.; Huang, C.-Y. Floating terahertz metamaterials with extremely large refractive index sensitivities. *Photon- Res.* **2021**, *9*, 1970. [CrossRef]
32. Yin, S.; Zhu, Z.; Gao, X.; Wang, Q.; Yuan, J.; Liu, Y.; Jiang, L. Terahertz nonreciprocal and functionality-switchable de-vices based on dielectric multilayers integrated with graphene and VO_2. *Opt. Lett.* **2022**, *47*, 678–681. [CrossRef]

33. Jacob, J.; Babu, A.; Mathew, G.; Mathew, V. Propagation of surface plasmon polaritons in anisotropic MIM and IMI structures. *Superlattices Microstruct.* **2008**, *44*, 282–290. [CrossRef]
34. Burke, J.J.; Stegeman, G.I.; Tamir, T. Surface-polariton-like waves guided by thin, lossy metal films. *Phys. Rev. B* **1986**, *33*, 5186–5201. [CrossRef] [PubMed]
35. Wu, L.; Che, K.; Xiang, Y.; Qin, Y.J. Enhancement of Sensitivity with High− Reflective− Index Guided− Wave Nanomateri-als for a Long− Range Surface Plasmon Resonance Sensor. *Nanomaterials* **2022**, *12*, 168. [CrossRef]
36. Johnson, P.B.; Christy, R.W. Optical Constants of the Noble Metals. *Phys. Rev. B* **1972**, *6*, 4370. [CrossRef]
37. Rakić, A.D.; Djurišić, A.B.; Elazar, J.M.; Majewski, M.L. Optical properties of metallic films for vertical-cavity optoelectronic devices. *Appl. Opt.* **1998**, *37*, 5271–5283. [CrossRef]
38. Abdellatif, S.; Ghannam, R.; Khalil, A.S.G. Simulating the dispersive behavior of semiconductors using the Lorentzian-Drude model for photovoltaic devices. *Appl. Opt.* **2014**, *53*, 3294–3300. [CrossRef]
39. Verma, R.; Gupta, B.D.; Jha, R.J. Sensitivity enhancement of a surface plasmon resonance based biomolecules sensor using graphene and silicon layers. *Sens. Actuators B Chem.* **2011**, *160*, 623–631. [CrossRef]
40. Sharma, A.K.; Gupta, B.D. On the performance of different bimetallic combinations in surface plasmon resonance based fiber optic sensors. *J. Appl. Phys.* **2007**, *101*, 093111. [CrossRef]
41. Economou, E.N. Surface Plasmons in Thin Films. *Phys. Rev.* **1969**, *182*, 539–554. [CrossRef]
42. Gupta, B.; Sharma, A.K. Sensitivity evaluation of a multi-layered surface plasmon resonance-based fiber optic sensor: A theoretical study. *Sens. Actuators B Chem.* **2005**, *107*, 40–46. [CrossRef]
43. Hansen, W. Electric fields produced by the propagation of plane coherent electromagnetic radiation in a stratified medium. *J. Opt. Soc. Am.* **1968**, *58*, 380–390. [CrossRef]
44. Maurya, J.B.; Prajapati, Y.K.; Singh, V.; Saini, J.P. Sensitivity enhancement of surface plasmon resonance sensor based on graphene–MoS2 hybrid structure with TiO_2–SiO_2 composite layer. *Appl. Phys. A* **2015**, *121*, 525–533. [CrossRef]
45. Sarid, D. Long-range surface-plasma waves on very thin metal films. *Phys. Rev. Lett.* **1981**, *47*, 1927. [CrossRef]
46. Wang, B.; Singh, S.C.; Lu, H.; Guo, C. Design of aluminum bowtie nanoantenna array with geometrical control to tune lspr from uv to near-ir for optical sensing. *Plasmonics* **2020**, *15*, 609–621. [CrossRef]
47. Lazareva, E.N.; Tuchin, V. Measurement of refractive index of hemoglobin in the visible/NIR spectral range. *J. Biomed. Opt.* **2018**, *23*, 035004. [CrossRef]
48. Chen, K.; Zhu, L.; Liu, Y.; Niu, H.; Dong, M.; Luo, F. Frequency-splitting effect of fiber laser for liquid refractive index-measurement. *Opt. Fiber Technol.* **2021**, *67*, 102719. [CrossRef]
49. Li, Z.; Zhang, Y.; Guo, X.; Tong, C.; Chen, X.; Zeng, Y.; Shen, J.; Li, C. Highly sensitive short-range mode resonance sensor with multilayer structured hyperbolic metamaterials. *Opt. Express* **2023**, *31*, 3520. [CrossRef]
50. Maurya, S.; Maurya, P.; Verma, R. Dual mode fiber optic high-performance sensor designs for ultra-low concentrations in NIR region. *Opt. Quantum Electron.* **2023**, *55*, 1–23. [CrossRef]
51. Vala, M.; Etheridge, S.; Roach, J.; Homola, J. Long-range surface plasmons for sensitive detection of bacterial analytes. *Sens. Actuators B Chem.* **2009**, *139*, 59–63. [CrossRef]
52. Zhao, Y.; Gan, S.; Wu, L.; Zhu, J.; Xiang, Y.; Dai, X. GeSe nanosheets modified surface plasmon resonance sensors for enhancing sensitivity. *Nanophotonics* **2020**, *9*, 327–336. [CrossRef]
53. Gao, Z.; Hou, Z.; Wang, H.; Tong, X.; Shen, J.; Li, C. High-Sensitivity Sensor Based on Energy Transfer. *IEEE Photon- Technol. Lett.* **2022**, *34*, 787–790. [CrossRef]